

nature photonics



SEPTEMBER 2015 VOL 9 NO 9
www.nature.com/naturephotonics

IMAGING

Wavefront shaping

NANOANTENNAS

Electrical drive

NONLINEAR OPTICS

Inverse four-wave mixing

Intracellular lasers

Intracellular microlasers

Matjaž Humar^{1,2} and Seok Hyun Yun^{1,3*}

Optical microresonators¹, which confine light within a small cavity, are widely exploited for various applications ranging from the realization of lasers² and nonlinear devices^{3–5} to biochemical and optomechanical sensing^{6–11}. Here we use microresonators and suitable optical gain materials inside biological cells to demonstrate various optical functions *in vitro* including lasing. We explore two distinct types of microresonator—soft and hard—that support whispering-gallery modes. Soft droplets formed by injecting oil or using natural lipid droplets support intracellular laser action. The laser spectra from oil-droplet microlasers can chart cytoplasmic internal stress ($\sim 500 \text{ pN } \mu\text{m}^{-2}$) and its dynamic fluctuations at a sensitivity of $20 \text{ pN } \mu\text{m}^{-2}$ (20 Pa). In a second form, whispering-gallery modes within phagocytized polystyrene beads of different sizes enable individual tagging of thousands of cells easily and, in principle, a much larger number by multiplexing with different dyes.

Luminescent probes, including fluorescent dyes and proteins, quantum dots, bioluminescent molecules and plasmonic nanoparticles, have become indispensable tools in the fields of cell biology and medical sciences. Although these molecular probes are immensely useful, their relatively broad emission spectra, typically in the range of 30–100 nm, limit the number of probes that are simultaneously usable without ambiguity and often make their spectra indistinguishable from the broad background emission of endogenous molecules in tissues. It is fundamentally challenging to engineer molecules with much narrower spontaneous emission¹². However, photonic principles such as optical resonance and stimulated emission allow spectral narrowing (filtering) via coherent loss or gain. The generation of narrowband resonant emission from biological cells has been demonstrated using cellular lasers with external cavities^{13,14} or photonic crystal needles¹⁵. Recently, we have sought to generate stand-alone cell lasers¹⁶, and we now describe effective approaches based on intracellular whispering-gallery mode (WGM) micro-resonators formed by soft and hard materials. WGMs are formed when light is circulating in a transparent spherical object as a result of being trapped due to total internal reflection at the interface. WGM cavities can have dimensions on the microscale or nanoscale¹⁷, although they are much larger than conventional luminescent probes.

We first describe soft WGM cavities in the form of oil droplets in cells. Nile red dye-mixed polyphenyl ether (PPE), a chemically inert optical grade fluid with low viscosity (100 cP) and a refractive index of $n = 1.69$ (Fig. 1a), was injected into the cells. The size of the droplets was controlled¹⁸ to fall within the range of 4–20 μm , corresponding to a volume of 30–4,000 fl (Supplementary Movie 1 and Fig. 1b). Droplets larger than 7 μm demonstrate lasing upon pulsed excitation ($\lambda = 535 \text{ nm}$, 5 ns, 10 Hz) with thresholds as low as a few nanojoules per pulse (Fig. 1c,d). This energy level is non-harmful for the cell^{13,14}. The instantaneous heating of a droplet is calculated to be $<1 \text{ }^\circ\text{C}$, and the ambient temperature increase in

the cytosol is negligible (Supplementary Section 3). When the droplet is under uniaxial stress, its shape deviates from a sphere and the deformation is manifested in the emission spectrum as a splitting of laser lines (Fig. 1e). For a small deformation the shape can be approximated as a spheroid, which supports laser oscillation in the equatorial plane (this has the lowest curvature and therefore the minimum optical loss). The modes were fitted to a model and the equatorial and polar semi-axes (a and b , respectively) were determined (Supplementary Section 1). From Laplace's law, the flattening stress $\Delta\sigma$ is related to the local mean curvature of the droplet surface¹⁹, $\Delta\sigma = 2\gamma\Delta H$, where γ is the surface tension and ΔH is the difference in the curvature (Supplementary Section 5). For small eccentricity e , that is, $e^2 \ll 1$, the stress is approximated as

$$\Delta\sigma \approx \frac{2\gamma}{a} e^2 \quad (1)$$

For the droplet in Fig. 1e we measured $a = 8.5$ and $b = 8.3 \mu\text{m}$, and, with $\gamma \approx 45 \text{ mN m}^{-1}$ for the oil/water interface, we determined $\Delta\sigma = 500 \text{ pN } \mu\text{m}^{-2}$. Time-lapse traces of the output spectra revealed dynamic variations of the cellular stress in live cells (Fig. 1f). The mean fluctuation of the internal stress was measured to be $\sim 150 \text{ pN } \mu\text{m}^{-2}$ (Fig. 1g). From the baseline fluctuation in dead cells ($\langle\Delta e^2\rangle = 0.19\%$), the force sensitivity is $\sim 20 \text{ pN } \mu\text{m}^{-2}$ (20 Pa), which is an order of magnitude better than obtained from direct image-based analysis¹⁹.

We next investigated whether cells naturally containing lipid droplets ($n = 1.47$) can support laser oscillation (Fig. 2a). Adipocytes freshly extracted from porcine subcutaneous tissue contain a single lipid droplet with nearly perfect spherical geometry (Fig. 2b,c). After incubation with a lipophilic fluorescent dye and pumping with a pulsed laser, the cells exhibited lasing with WGM outputs (Fig. 2d) and a distinct threshold (Fig. 2e), thus demonstrating a completely natural intracellular optical cavity. Next, we examined the possibility of generating lasing from adipocytes *in situ* in tissues. Adipocytes in fat are closely packed and have random shapes (Fig. 2f), which have a lower cavity Q -factor and require a higher pump energy for lasing. To lower the threshold we injected a mixture of collagenase and lipophilic Nile red dye into the subcutaneous fat. The collagenase releases adipocytes from the tissue matrix, and they acquire spherical shapes²⁰. An optical fibre was inserted through a needle puncture hole to excite the adipocytes with pulsed laser light and to collect the light emitted from the tissue (Fig. 2g). The adipocytes near the fibre tip readily showed lasing (Fig. 2h). In some cases, adipocytes at the periphery of the fat tissue (with a more round shape) also showed lasing (Supplementary Fig. 1), eliminating the need for collagenase.

Solid microspheres (such as polystyrene microspheres) offer a simple way to devise non-deformable, intracellular lasers (Fig. 3a). Polystyrene beads are readily internalized by endocytosis^{21,22} (Fig. 3b). We have observed that both macrophages and

¹Wellman Center for Photomedicine, Harvard Medical School, Massachusetts General Hospital, 65 Landsdowne Street UP-5, Cambridge, Massachusetts 02139, USA. ²Condensed Matter Department, J. Stefan Institute, Jamova 39, Ljubljana SI-1000, Slovenia. ³Harvard-MIT Health Sciences and Technology, 77 Massachusetts Avenue Cambridge, Cambridge, Massachusetts 02139, USA. *e-mail: syun@hms.harvard.edu

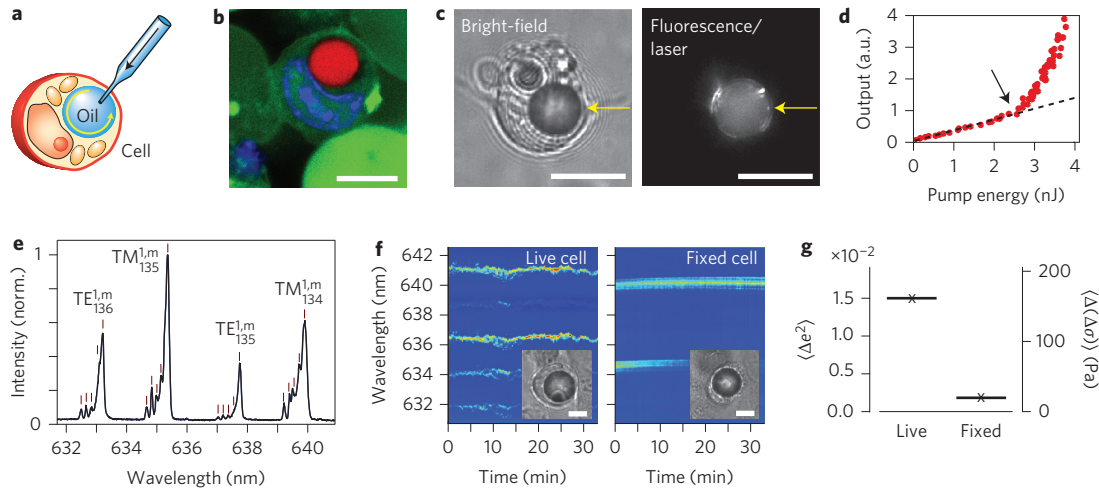


Figure 1 | Injected oil droplet laser. **a**, Schematic of the injection of oil into the cytoplasm of a cell. **b**, Confocal fluorescence image of a cell with a PPE droplet doped with Nile red dye (red). The cell nucleus (blue) became kidney-shaped, giving space to the droplet. **c**, Bright-field (left) and laser-output (right) images of a cell with a droplet (arrows) above the lasing threshold. **d**, Output light intensity from a droplet as a function of pump pulse energy, showing a distinct laser threshold (arrow). Dashed line: linear fit to the fluorescence output below threshold. **e**, A typical output spectrum of the lasing modes. All modes are first radial modes, two modes with TE polarization and two with TM. Each mode is split into multiple submodes. From their splitting in these data, the spheroid is determined to be of oblate shape with equatorial and polar semi-axes measuring 8.3 and 8.5 μm , respectively. **f**, Time-lapse variation of the output spectrum for a live cell (left) and a dead cell fixed with formaldehyde (right). **g**, Standard deviation of the square of eccentricity and corresponding internal stress for live and fixed (dead) cells. Scale bars (**b,c,f**), 10 μm .

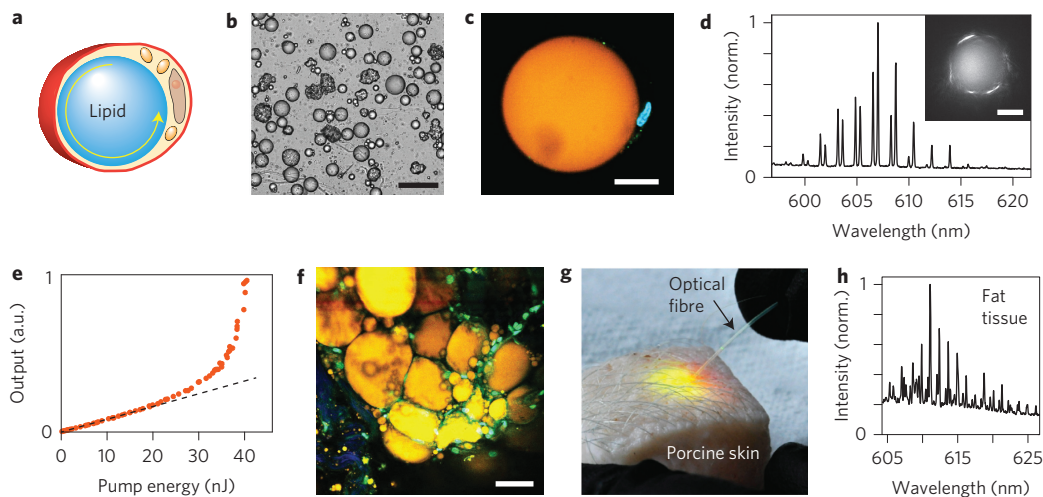


Figure 2 | Adipocyte lasers. **a**, Illustration of a typical mature subcutaneous adipocyte with a lipid droplet. **b**, Individual adipocytes extracted from subcutaneous porcine fat. **c**, Confocal image of an adipocyte containing a large lipid droplet (orange), which occupies the majority of the cell volume. The nucleus (blue) is visible next to the droplet. **d**, Spectrum from a 45 μm adipocyte above lasing threshold, showing typical WGM spectral peaks. Inset: fluorescence image of the cell above lasing threshold. **e**, Output energy as a function of pump energy. Dashed line: linear fit to the fluorescence output below laser threshold. **f**, Two-photon confocal image of adipocytes *in situ* in subcutaneous fat tissue, after intradermal injection of Nile red dye (yellow). **g**, Generation of cellular laser emission from within tissue. The pump laser is fibre-optically guided into the subcutaneous fat layer after injecting a mixture of collagenase and Nile red dye. **h**, Spectrum of light collected by the optical fibre from the tissue. Scale bars, 200 μm (**b**) and 20 μm (**c,d,f**).

non-phagocytic cells (such as HeLa and NIH3T3) engulf beads up to 20 μm in diameter (d), large enough to exhibit lasing at low pump energy. The viability of HeLa cells 24 h after engulfing one or more polystyrene beads ($>6 \mu\text{m}$) was $98.4 \pm 0.6\%$ (compared to $99.4 \pm 0.2\%$ for cells without beads). WGM lasers offer multiple options for the position of the gain medium, including inside the resonator, outside the resonator and on the surface of the bead. We tested all three cases. First, fluorescent dye-embedded polystyrene beads provided gain within the beads. Beads larger than $d = 11 \mu\text{m}$ supported lasing inside the cells at pump energy levels below a few nanojoules (Fig. 3c,d and Supplementary Fig. 2).

The bead surface can also be functionalized with probe molecules such as antibodies or DNA for intracellular molecular sensing^{6–11}. In the second case, the cell tracker dye 5-chloromethylfluorescein diacetate (CMFDA), which is retained in the cytosol, served as the gain medium for BaTiO₃ beads. Lasing was observed in beads with dimensions as small as 8 μm (Fig. 3e). The gain medium interacts freely with the cell, generating amplified signals modulated by the cavity resonance. Third, the surfaces of high-index ($n = 1.9$) BaTiO₃ beads were coated with fluorescent dye (Alexa Fluor 488). Although a monolayer of dye did not provide enough gain for lasing, its emission spectrum was strongly

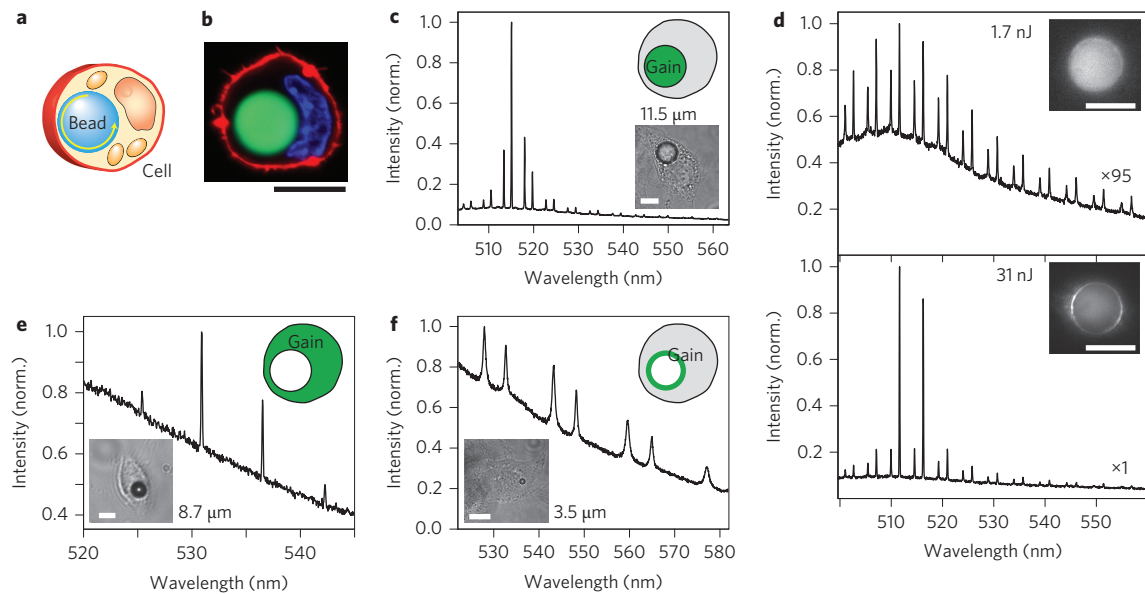


Figure 3 | Three different types of solid intracellular microcavity. **a**, Schematic of a bead inside a cell. **b**, Confocal fluorescence image of a HeLa cell containing a polystyrene bead (green), nucleus (blue) and plasma membrane (red). **c**, Laser emission from a fluorescent polystyrene bead inside a cell. **d**, Emission spectra and images (insets) of a fluorescent polystyrene bead below (top) and above (bottom) lasing threshold (3.2 nJ). **e**, Laser output from a 8.7 μm non-fluorescent BaTiO_3 bead embedded in a cell containing CMFDA dye in its cytoplasm. **f**, Spontaneous emission from a 3.5 μm BaTiO_3 bead coated with Alexa 488 dye below laser threshold. Scale bars, 10 μm .

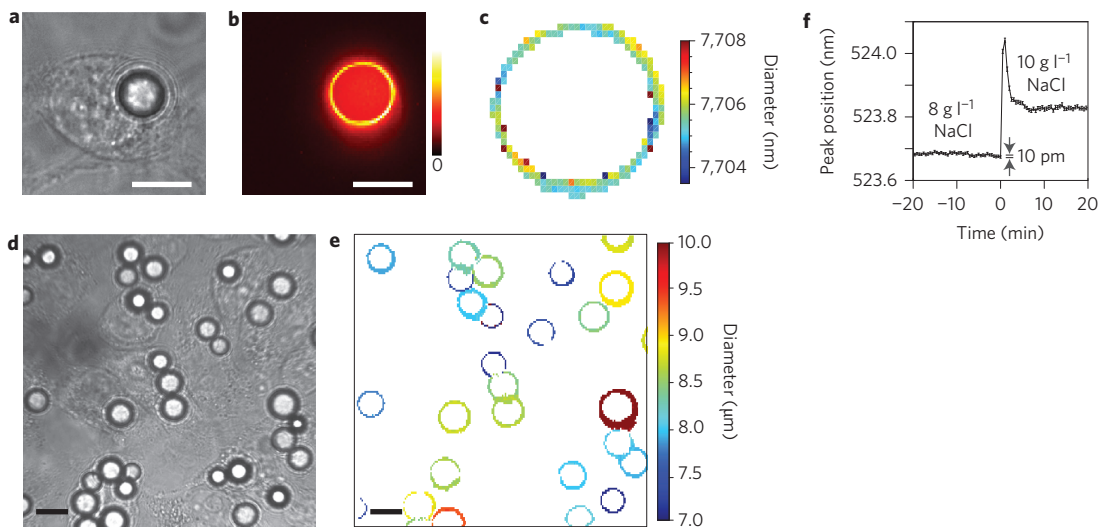


Figure 4 | Tagging and sensing applications of solid intracellular microcavities. **a**, Bright-field image of a HeLa cell containing a polystyrene fluorescent bead. **b**, False-colour image of the cell in **a**, showing the intensity of the oscillating WGMs. **c**, A bead diameter map calculated from confocal hyperspectral images of the WGM output. **d, e**, Multiple HeLa cells containing beads (**d**) and the corresponding bead diameter map (**e**). **f**, Time-lapse measurements of a resonant peak from a glass bead inside a HeLa cell. The addition of 2 g l^{-1} sodium chloride at $t = 0$ caused the peak wavelength to shift. Scale bars, 10 μm .

modulated by high-Q (700) resonance in beads with dimensions down to $d = 3.5 \mu\text{m}$, with relatively low fluorescence background (Fig. 3f). Any combinations of the three gain locations are of course possible. Furthermore, the gain and sensing media may be co-located or separated.

The precise wavelengths of the multiple spectral peaks from a bead above or below lasing threshold (Fig. 3) are uniquely determined by the size of the bead. We measured the output spectra from fluorescent polystyrene beads from each spatial location in a mid-plane of the cell (Fig. 4a) in a confocal hyperspectral imaging set-up with a numerical aperture of 1.25 and continuous-wave pumping with a 455 nm light-emitting diode (LED). A spatial

map of the intensity of the resonance peaks has a ring shape (Fig. 4b), representing light circulating in the bead and leaking out in the tangential direction. By fitting the spectra with WGM theory²³, the effective bead diameter d was calculated at each pixel. The diameter around the circumference varies by 1–2 nm, which may reflect the deviation of the actual bead from a perfect sphere (Fig. 4c). The precision of the mean diameter is $\sim 50 \text{ pm}$ (Supplementary Fig. 3), which indicates a remarkable sensitivity of the WGM analysis ($50 \text{ pm}/7.7 \mu\text{m} = 6.5 \times 10^{-6}$). The same type of analysis can be done for beads operated above threshold by pulsed pumping. However, when the number of lasing modes is less than three to four, the size measurement is frustrated or has

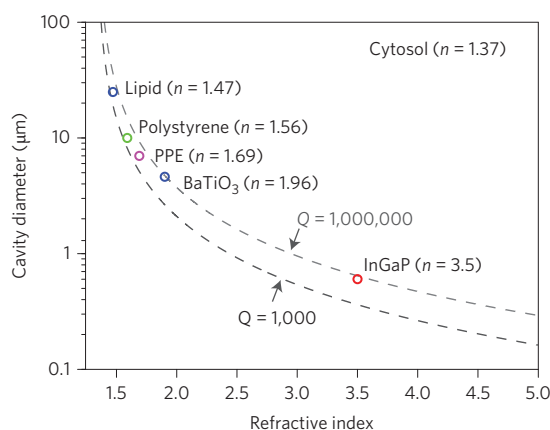


Figure 5 | Size of intracellular microlasers. Q-factors of WGMs are highly dependent on the refractive index and cavity size. The two dashed lines represent theoretical calculations of two Q-factors: 10^6 and 10^3 , respectively. Circles indicate the measured minimum size of laser achieved inside a cell for a lipid droplet in an adipocyte, a polystyrene bead and a PPE droplet inside a HeLa cell, and BaTiO₃ beads in 15 mM pyrromethene solution, as well as InGaP disk lasers in air²⁸.

an error of as much as one to two free spectral ranges (~100 nm) (Supplementary Fig. 4).

An intriguing application of this precision measurement is to use beads with different diameters to tag individual cells (Fig. 4d,e; Supplementary Fig. 5 and Supplementary Movie 2). The diameter interval between beads should be large enough to accommodate the typical wavelength variation of 2 nm due to refractive index changes arising from intracellular dynamics ($\Delta\lambda/\lambda \approx \Delta n/n + \Delta d/d$), where n is the effective refractive index for the oscillating mode. With polydispersed beads with dimensions falling in the range 8–12 μm and a bin size of 2 nm, we can distinguish 2,000 individual beads. By using different fluorescent dyes with distinct emission bands this number can easily be increased several fold. Furthermore, each cell can engulf multiple particles (Supplementary Fig. 6b). Using three beads per cell and five different fluorescence dyes with non-overlapping spectra, it would be possible to individually tag $^{2,000 \times 5} C_3 = 2 \times 10^{11}$ cells, which is comparable to the number of cells in the human body and many orders of magnitude greater than achievable using state-of-the-art techniques such as stochastic brainbow recombination²⁴ for *in vivo* cell tracking, or high-throughput on-chip cytometry and cell-based analysis.

To demonstrate intracellular sensing we measured the spectral changes of soda lime glass beads coated with Alexa Fluor 488 in HeLa cells, while the cell culture medium was provided with an additional 2 g l⁻¹ of sodium chloride. Exposure of cells to hypertonic solution causes intracellular water to quickly diffuse out of the cell, reducing the cell volume. The shrinking is followed by a partial recovery via a regulatory volume increase²⁵. The change in cell volume changes the concentration of the molecules in the cytoplasm, thereby also changing the refractive index. The time dependence of the shift in the position of a WGM (Fig. 4f) corresponds to $\Delta n \approx 1.0 \times 10^{-2}$, which is close to the value of 7.6×10^{-3} calculated using the Boyle-van't Hoff law (Supplementary Section 6). As a control experiment, the same volume of medium was added without changing the osmolarity, and produced no response (Supplementary Fig. 7).

In this Letter we have demonstrated stand-alone cell lasers by using an intracellular WGM microresonator, a dye gain medium and far-field optical pumping with nanosecond pulses. A pulse duration of 100 ps could reduce the threshold pump energy (by ~50 times) while supporting distinct WGM modes in the

microresonators. The shape of the intracellular WGM cavities is not limited to spheres—cylinders, toruses and disks can also be used. The micrometre size may offer flexibility in cavity engineering for specific mode selection or direction-dependent radiation²⁶. Biodegradable polymers²⁷ may improve biocompatibility, and the use of smaller cavities causing minimal perturbations in cells would also be useful. High-refractive-index materials, such as semiconductors ($n > 3$)²⁸ or the realization of metamaterials with extremely high refractive indices²⁹ should enable the creation of sub-micrometre WGM lasers (Fig. 5). Plasmon-based spasers can have dimensions as small as tens of nanometres³⁰, but the WGM analysis demonstrated here is most effective with microresonators accommodating multiple optical wavelengths.

Methods

Methods and any associated references are available in the online version of the paper.

Received 31 March 2015; accepted 26 June 2015; published online 27 July 2015

References

- Vahala, K. J. Optical microcavities. *Nature* **424**, 839–846 (2003).
- Qian, S. X., Snow, J. B., Tzeng, H. M. & Chang, R. K. Lasing droplets—highlighting the liquid–air interface by laser-emission. *Science* **231**, 486–488 (1986).
- Hill, M. T. *et al.* A fast low-power optical memory based on coupled micro-ring lasers. *Nature* **432**, 206–209 (2004).
- Kippenberg, T. J., Holzwarth, R. & Diddams, S. A. Microresonator-based optical frequency combs. *Science* **332**, 555–559 (2011).
- Spillane, S. M., Kippenberg, T. J. & Vahala, K. J. Ultralow-threshold Raman laser using a spherical dielectric microcavity. *Nature* **415**, 621–623 (2002).
- Armani, A. M., Kulkarni, R. P., Fraser, S. E., Flagan, R. C. & Vahala, K. J. Label-free, single-molecule detection with optical microcavities. *Science* **317**, 783–787 (2007).
- Vollmer, F. & Arnold, S. Whispering-gallery-mode biosensing: label-free detection down to single molecules. *Nature Methods* **5**, 591–596 (2008).
- Zhu, J. G. *et al.* On-chip single nanoparticle detection and sizing by mode splitting in an ultrahigh-Q microresonator. *Nature Photon.* **4**, 46–49 (2010).
- Fan, X. D. & White, I. M. Optofluidic microsystems for chemical and biological analysis. *Nature Photon.* **5**, 591–597 (2011).
- Baaske, M. D., Foreman, M. R. & Vollmer, F. Single-molecule nucleic acid interactions monitored on a label-free microcavity biosensor platform. *Nature Nanotech.* **9**, 933–939 (2014).
- Himmelhaus, M. & Francois, A. *In-vitro* sensing of biomechanical forces in live cells by a whispering gallery mode biosensor. *Biosens. Bioelectron.* **25**, 418–427 (2009).
- Zhang, J., Campbell, R. E., Ting, A. Y. & Tsien, R. Y. Creating new fluorescent probes for cell biology. *Nature Rev. Mol. Cell Biol.* **3**, 906–918 (2002).
- Gather, M. C. & Yun, S. H. Single-cell biological lasers. *Nature Photon.* **5**, 406–410 (2011).
- Jonáš, A. *et al.* *In vitro* and *in vivo* biolasing of fluorescent proteins suspended in liquid microdroplet cavities. *Lab. Chip* **14**, 3093–3100 (2014).
- Shambat, G. *et al.* Single-cell photonic nanocavity probes. *Nano Lett.* **13**, 4999–5005 (2013).
- Fan, X. & Yun, S.-H. The potential of optofluidic biolasers. *Nature Methods* **11**, 141–147 (2014).
- Hill, M. T. & Gather, M. C. Advances in small lasers. *Nature Photon.* **8**, 908–918 (2014).
- Zhang, Y. & Yu, L. C. Microinjection as a tool of mechanical delivery. *Curr. Opin. Biotechnol.* **19**, 506–510 (2008).
- Campàs, O. *et al.* Quantifying cell-generated mechanical forces within living embryonic tissues. *Nature Methods* **11**, 183–189 (2014).
- Gardan, D., Gondret, F. & Louveau, I. Lipid metabolism and secretory function of porcine intramuscular adipocytes compared with subcutaneous and perirenal adipocytes. *Am. J. Physiol. Endocrinol. Metab.* **291**, E372–E380 (2006).
- Cannon, G. J. & Swanson, J. A. The macrophage capacity for phagocytosis. *J. Cell Sci.* **101**, 907–913 (1992).
- Kobayashi, S. *et al.* Artificial induction of autophagy around polystyrene beads in nonphagocytic cells. *Autophagy* **6**, 36–45 (2010).
- Gorodetsky, M. L. & Fomin, A. E. Geometrical theory of whispering-gallery modes. *IEEE J. Sel. Topics Quantum Electron.* **12**, 33–39 (2006).
- Livek, J. *et al.* Transgenic strategies for combinatorial expression of fluorescent proteins in the nervous system. *Nature* **450**, 56–62 (2007).
- Schultz, S. G. *Molecular Biology of Membrane Transport Disorders* (Springer, 1996).

26. Wang, Q. J. *et al.* Whispering-gallery mode resonators for highly unidirectional laser action. *Proc. Natl Acad. Sci. USA* **107**, 22407–22412 (2010).
27. Nizamoglu, S., Gather, M. C. & Yun, S. H. All-biomaterial laser using vitamin and biopolymers. *Adv. Mater.* **25**, 5943–5947 (2013).
28. Zhang, Z. *et al.* Visible submicron microdisk lasers. *Appl. Phys. Lett.* **90**, 111119 (2007).
29. Choi, M. *et al.* A terahertz metamaterial with unnaturally high refractive index. *Nature* **470**, 369–373 (2011).
30. Stockman, M. I. Spasers explained. *Nature Photon.* **2**, 327–329 (2008).

Acknowledgements

This research was supported in part by the US National Science Foundation (NSF; ECCS-1101947, EEC-1358296, ECCS-1505569) and the National Institutes of Health (P41 EB015903). M.H. was supported in part by the Marie Curie International Outgoing Fellowship no. 627274 within the 7th European Community Framework Programme. The authors thank J. Zhao and Wellman Centre Photopathology Core for technical

support. Part of this work was performed at the Centre for Nanoscale Systems (CNS) at Harvard University, which is a member of the National Nanotechnology Infrastructure Network (NNIN) and supported by the NSF under award no. ECS-0335765.

Author contributions

M.H. and S.H.Y. designed the study. M.H. carried out the experiments and analysed the data. M.H. and S.H.Y. wrote the manuscript.

Additional information

Supplementary information is available in the [online version](#) of the paper. Reprints and permissions information is available online at www.nature.com/reprints. Correspondence and requests for materials should be addressed to S.H.Y.

Competing financial interests

The authors declare no competing financial interests.

Methods

Optical set-up. For the pumping of the cell lasers and the collection of light, a $\times 40$ 1.25 NA or $\times 100$ 1.40 NA oil immersion objective was used. Pumping was achieved using an optical parametric oscillator with 5 ns pulse duration, tuned to 475 nm for green dyes or 535 nm for red dyes. The laser beam was slightly divergent at the objective entrance pupil, so the focus at the sample was located slightly further away from the objective focal plane, and the beam diameter at the objective focal plane was ~ 20 μm wide. For measurements of polystyrene microsphere modes below the laser threshold (Fig. 4), a 455 nm LED was used as the excitation source. The collected light was sent through a dichroic mirror and split 50:50 into a charge-coupled device camera and an imaging spectrometer (300 mm focal length, 0.05 nm resolution). For all measurements except for the hyperspectral imaging, the spectrum was collected through the entrance slit of the spectrometer and therefore represents an integration along a line crossing the centre of a bead or droplet. For hyperspectral imaging the spectrometer slit was replaced by a 10 μm pinhole, and a two-dimensional raster scan was performed with an acquisition time of 0.1 s per pixel. The spectral peaks above a broad fluorescence background were integrated to obtain the laser intensity image shown in Fig. 4b. The individual spectral peaks after subtracting the background were fitted with a Lorentzian curve to obtain their central wavelengths, which were subsequently fitted to Supplementary equation (1), with $a = b$.

Cell culture. HeLa, NIH3T3 and RAW 264.7 cell lines were grown at 37 °C with 5% CO₂ in full growth medium (Dulbecco's modified Eagle medium supplemented with 10% fetal bovine serum and 1% pen-strep). The cells were incubated in full growth medium supplied with beads for 12 h before laser experiments. The viability assay was performed 24 h after the cells were injected with PPE or were supplied with beads using ethidium homodimer-1.

Oil injection. Non-toxic, low-viscosity high-index polyphenyl ether oil (PPE, SL-5267, Santolubes) was doped with 5 mM Nile red (9-diethylamino-5-benzo[α]phenoxazinone) before injection into HeLa and NIH3T3 cells. The

injection was performed using a microinjector (FemtoJet, Eppendorf) and a glass micropipette with a 1.0 μm outer diameter (Femtotip, Eppendorf). The size of the injected droplets was controlled by the injection time (ranging from 0.2 s to 1 s), with an injection pressure of 1,700 kPa.

Adipocytes. Fresh subcutaneous fat tissue was collected from the neck of a two-month-old pig, minced, and mixed with an equal volume of phosphate buffered saline (PBS) containing 2 mg ml⁻¹ collagenase (type 1A). The mixture was incubated with frequent shaking at 37 °C for 30 min. The suspension was filtered through 250 μm nylon mesh to remove undigested tissue and centrifuged at 65g for 5 min to collect the top layer of fat. The adipocytes were stained by adding 1% 10 mM Nile red in acetone. In the tissue laser experiments, 1 ml PBS containing 1 mg ml⁻¹ collagenase and 1% of 10 mM Nile red in acetone was injected into the subcutaneous porcine fat. The tissue was incubated at 37 °C for 15 min. For excitation and light collection a multimode fibre with a core diameter of 200 μm was used.

Fluorescent beads. Three different bead types were used: 8 μm mean diameter green fluorescent polystyrene spheres (Thermo Scientific, Fluoro-Max, 18% coefficient of variation), 15–19 μm soda lime glass beads (Cospheric) and polydisperse BaTiO₃ beads with a broad size distribution of 1–40 μm (GL0175B, Mo-Sci). Polystyrene beads were incubated for 30 min at room temperature in 1 wt% poly-L-lysine hydrobromide ($M_w = 30,000$ – $70,000$) in water and washed three times. Soda lime and BaTiO₃ spheres were coated with Alexa Fluor 488 tetrafluorophenyl (TFP) ester dye (Life Technologies) as follows. Beads were washed with acetone and incubated in acetone containing 2% vol/vol 3-aminopropyltriethoxysilane for 15 min with mixing. The beads were washed twice with acetone, once with water, and dried at 120 °C for 30 min. The beads were redispersed in 0.1 M sodium bicarbonate buffer, pH 9.0. Alexa Fluor TFP ester (100 μg) dissolved in 10 μl dimethyl sulphoxide was added to a 200 μl bead dispersion in sodium bicarbonate buffer. After 2 h incubation, the beads were washed five times with water and transferred to PBS. All the above washing steps were performed by centrifugation at 5,000g for 5 min and with exchange of the medium.

Intracellular microlasers

Matjaž Humar^{1,2} and Seok Hyun Yun^{1,3*}

¹ Wellman Center for Photomedicine, Harvard Medical School, Massachusetts General Hospital, 65 Landsdowne St. UP-5, Cambridge, Massachusetts 02139, USA

² Condensed Matter Department, J. Stefan Institute, Jamova 39, SI-1000 Ljubljana, Slovenia

³ Harvard–MIT Health Sciences and Technology, Cambridge, 77 Massachusetts Avenue Cambridge, Massachusetts 02139, USA

*Corresponding author. E-mail: syun@hms.harvard.edu

1. Positions of resonances for whispering-gallery modes (WGMs)

Whispering-gallery modes can be uniquely characterized by a set of three mode numbers, the radial mode number q , the polar mode number l , the azimuthal mode number m and the polarization p . In spherical cavities the modes with different azimuthal mode numbers are degenerate, however deformation from spherical shape leads to mode splitting. For a prolate or oblate spheroid the frequencies of WGMs can be approximately calculated using an asymptotic expansion¹

$$n_s k a = l - \alpha_q \left(\frac{l}{2}\right)^{1/3} + \frac{2g(a-b) + a}{2b} - \frac{\chi n_r}{\sqrt{n_r^2 - 1}} + \frac{3\alpha_q^2}{20} \left(\frac{l}{2}\right)^{-1/3} - \frac{\alpha_q}{12} \left(\frac{2g(a^3 - b^3) + a^3}{b^3} + \frac{2\chi n_r(2\chi^2 - 3n_r^2)}{(n_r^2 - 1)^{3/2}}\right) \left(\frac{l}{2}\right)^{-2/3} \quad (1)$$

where

$$\chi = \begin{cases} 1 & \text{for TE modes} \\ 1/n_r & \text{for TM modes,} \end{cases}$$

a and b are equatorial and polar semi-axes of the spheroid, k is wavenumber, $l \gg 1$, $g = l - |m| = 0, 1, 2, \dots$ and $q = 1, 2, 3, \dots$ are mode numbers, α_q are negative q -th zeroes of the Airy function and $n_r = n_s/n_a$ is relative refractive index, where n_s is the refractive index of the spheroid and n_a is the index of the surrounding medium.

For the case (Fig. 1e-g) of a polyphenyl ether oil (PPE) droplet with 17 μm in diameter ($l \approx 135$), the relative error between the approximate equation (1) and an exact solution for the mode wavelength¹ is less than 2×10^{-4} , which corresponds to a diameter error of ~ 2 nm. The spheroid semi-axes were fitted to the experimental spectra to assuming $l \gg g$ and that the modes are adjacent to equatorial plane.

2. Free spectral ranges (FSRs) and Q-factors of WGM cavities inside cells

FSRs for different beads and droplets can be estimated from the measured diameters from their optical images and refractive indices given by the manufacturer or from literature. These values are compared to the FSR values measured from the optical spectra, as follows.

Adipocyte cell (Fig. 2d): estimated FSR: 1.79 nm, measured FSR: 1.76 nm

Polystyrene bead (Fig. 3c): estimated FSR: 4.73 nm, measured FSR: 4.63 nm

BaTiO₃ bead (Fig. 3d): estimated FSR: 5.57 nm, measured FSR: 5.56 nm

BaTiO₃ bead (Fig. 3e): estimated FSR: 14.0 nm, measured FSR: 15.1 nm

Small discrepancies between estimated and measured FSRs are mainly due to error in measuring the diameter of the beads from their microscope images and from the discrepancy between their real refractive index and the assumed values.

Q-factor of a sphere with finite radiative loss can be approximated as²

$$Q \approx \frac{1}{2} \left(l + \frac{1}{2}\right) n_r^{1-2k} (n_r^2 - 1)^{1/2} e^{2T} \quad (2)$$

where

$$T = \left(l + \frac{1}{2}\right) (\eta - \tanh \eta)$$

$$\cosh \eta = n_r \left[1 - \frac{1}{l + 1/2} \left(\alpha_q \beta + \frac{n_r^{1-2k}}{\sqrt{n_r^2 - 1}} \right) \right]^{-1}$$

$$\beta = \left[\frac{1}{2} \left(l + \frac{1}{2} \right) \right]^{1/3}$$

and

$$k = \begin{cases} 0 & \text{for TE modes} \\ 1 & \text{for TM modes.} \end{cases}$$

For a 10.3- μm polystyrene bead in water, the theoretical Q-factor calculated using (2) is 20,400. Our measurement of a bead immersed in pure water showed $Q = 5,000$. The resolution of our spectrometer was 0.1 nm, which limits the maximum Q-factor that can be measured to $\sim 5,000$. For the same polystyrene bead in a cell, the calculated Q-factor is 18,100, whereas our measurement of a bead inside a live cell indicated $Q = 2,100$. A Q-factor of 2,100, the intracavity light makes about 5.5 round trips before the energy decays to $1/e$ (37%) of its initial value. The fractional power loss per round trip is 17%.

3. Heating and temperature rise by a micro-laser

The total pump energy absorbed by a microsphere or droplet depends on the size and concentration of the fluorescent dyes it contains. Since the extinction coefficients of fluorescent dyes are typically 50,000-90,000 $\text{M}^{-1}\text{cm}^{-1}$, a bead that has a diameter of greater than 10 μm and dyes at a concentration of 1 mM absorbs $>70\%$ of incident pump energy. Of the total absorbed energy, a fraction of it is converted into heat, which is given by one minus quantum yield (QY). With typical QY of 0.5-0.7, 30 to 50% of absorbed energy turns into heat. At pump pulse energy of 1 nJ onto the area matching the size of a microresonator, assuming 90% is absorbed and 50% of it is converted to heat, the total heat energy produced is 0.45 nJ.

Case I: for an oil droplet with a size of 20 μm (3.8 ng) and a specific heat of $1.8 \text{ J g}^{-1} \text{ }^\circ\text{C}^{-1}$, pump energy of 10 nJ on the droplet (i.e. 3.1 mJ/cm^2 in fluence) produces heat energy of 4.5 nJ and causes a temperature increase of $\Delta T = 0.7 \text{ }^\circ\text{C}$.

Case II: for a polystyrene bead with a size of 10 μm (0.52 ng) and a specific heat of $1.4 \text{ J g}^{-1} \text{ }^\circ\text{C}^{-1}$, pump energy of 1 nJ on the bead (i.e. 1.3 mJ/cm^2 in fluence) generates heat energy of 0.45 nJ and a temperature rise of $\Delta T = 0.6 \text{ }^\circ\text{C}$.

In both cases, heat diffusion to the surrounding medium (water) is negligible due to the short duration (5-10 ns) of the pump pulse. In the experiment, the period of pump pulse was 0.1 s, long enough for the heat deposit in the microresonator is fully dissipated to the surrounding. Therefore, the equilibrium temperature of the surrounding, which serves as heat reservoir, would be little affected. ΔT calculated above represents merely a peak rise that persists for a short ($< 1 \mu\text{s}$) duration of time. A peak rise of 10-20 $^\circ\text{C}$ may cause the degradation of some proteins in

close distance ($<1 \mu\text{m}$). It is highly unlikely that the short-lasting temperature rise will cause cytotoxicity. Nonetheless, the temperature rise during the operation of intracellular laser is an important factor to consider to avoid detrimental biological effects or in the interpretation of the output characteristics.

4. Sensitivity of WGMs to temperature and external refractive index change

For tagging application, the sensitivity of the resonance frequencies of a microresonator to the ambient temperature must be considered. The sensitivity to temperature of polystyrene beads can be estimated from the material properties of polystyrene. The coefficient of linear expansion of polystyrene is 7 to $8 \times 10^{-5}/^\circ\text{C}$ and, its relative index change is $-8.2 \times 10^{-5}/^\circ\text{C}$. Therefore, these two effects almost cancel out each other. Indeed, our measurements show a mode shift of only $3 \text{ pm}/^\circ\text{C}$ for a bead immersed in pure water. This corresponds to a diameter error of $60 \text{ pm}/^\circ\text{C}$ for a $10 \mu\text{m}$ bead. This temperature-dependent effect is well within the proposed diameter interval of 2 nm . We note that in mammalian cells in culture or *in vivo*, the ambient temperature is kept constant at 37°C within few degrees.

WGMs are also sensitive to changes in external refractive index. However, the variation is orders of magnitude less than 2 nm in most practical applications when high-index beads are used. Furthermore, the mode shifts caused by change in outside refractive index could be entirely eliminated by coating the beads with low refractive index cladding.

5. Droplet deformation and intracellular force measurement

Spheroid eccentricity is defined as

$$e = \sqrt{\frac{a^2 - b^2}{a^2}} \quad \text{for oblate spheroid, } a > b, \text{ or} \tag{3}$$

$$e = \sqrt{\frac{b^2 - a^2}{b^2}} \quad \text{for prolate spheroid, } a < b.$$

The semi-axes a and b are calculated from the mode splitting for different time points in Fig. 1f. The average eccentricities for live and dead cells (Fig. 1f) are 0.25 and 0.23 , respectively. Laplace's law is used to calculate approximate force acting on the droplet:

$$\Delta\sigma = \delta\sigma_1 - \delta\sigma_2 = 2\gamma(H_1 - H_2), \tag{4}$$

where $\delta\sigma_1$ and $\delta\sigma_2$ are the asymmetric components of the normal stress at the equator and the pole, respectively, and H_1 and H_2 are local curvatures of the equator and pole, respectively, given by $H_1 = (a^2 + b^2)/(2ab^2)$ and $H_2 = b/a^2$. When $a \approx b$ (i.e. $e^2 \ll 1$),

$$H_1 - H_2 \approx \frac{e^2}{a} \approx 2 \frac{a-b}{a^2} \tag{5}$$

In this case, equation (4) leads to $\Delta\sigma = (4\gamma/a)f$, where $f = (a-b)/a$ denotes the flattening of the spheroid or the relative difference between the semi-major and minor axes.

6. Intracellular sensing

Alexa Fluor 488 coated soda lime glass beads were incubated with HeLa cells as described above. A cell containing a single bead was illuminated by the 455-nm blue LED and the spectrum was recorded every 30 s. After 20 min, 25 μ L of pre-warmed PBS supplied with 160 g/L NaCl was mixed into 2 mL of full growth medium containing the cells. The final concentration of NaCl therefore increased from 8 g/L to 10 g/L. Shortly after the cells are exposed to the change in the osmolarity they can be approximated as ideal osmometers following Boyle-van't Hoff law. When changing the osmotic pressure from an initial value Π_0 to Π , the cell volume can be written as

$$V = \frac{\Pi_0}{\Pi}(V_0 - b) + b \quad (6)$$

where V_0 is the initial cell volume and b is the non-water fraction of cell volume. In our experiment, the osmolarity is changed from 298 mOsm/L to 366 mOsm/L. For HeLa cells³ $b/V_0 = 0.16$ and the calculated decrease in volume is 16%. The new refractive index of the cell cytoplasm n can be calculated from the initial refractive index⁴ $n_0 = 1.37$ and the relative volume change as

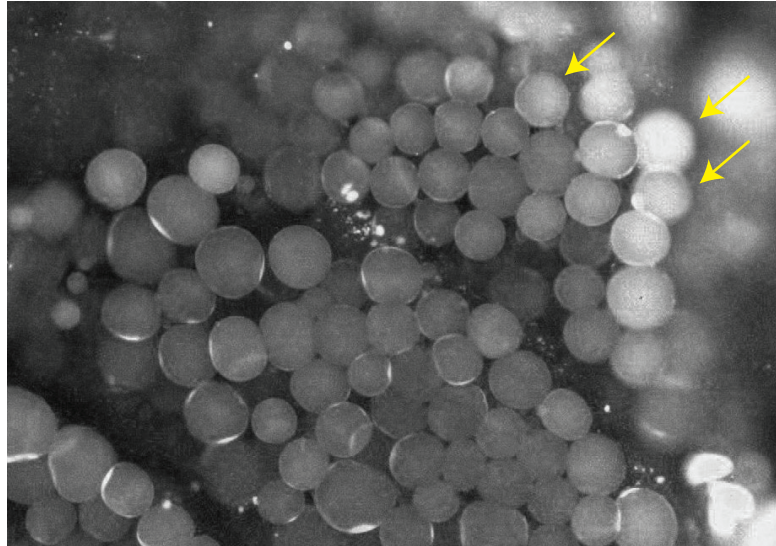
$$\frac{n_0 - n_w}{n - n_w} = \frac{c_0}{c} = \frac{V}{V_0} \quad (7)$$

where n_w is the refractive index of water and c_0 and c are the initial and final concentrations of the solutes in the cell. The change in refractive index calculated from the volume change is 7.6×10^{-3} .

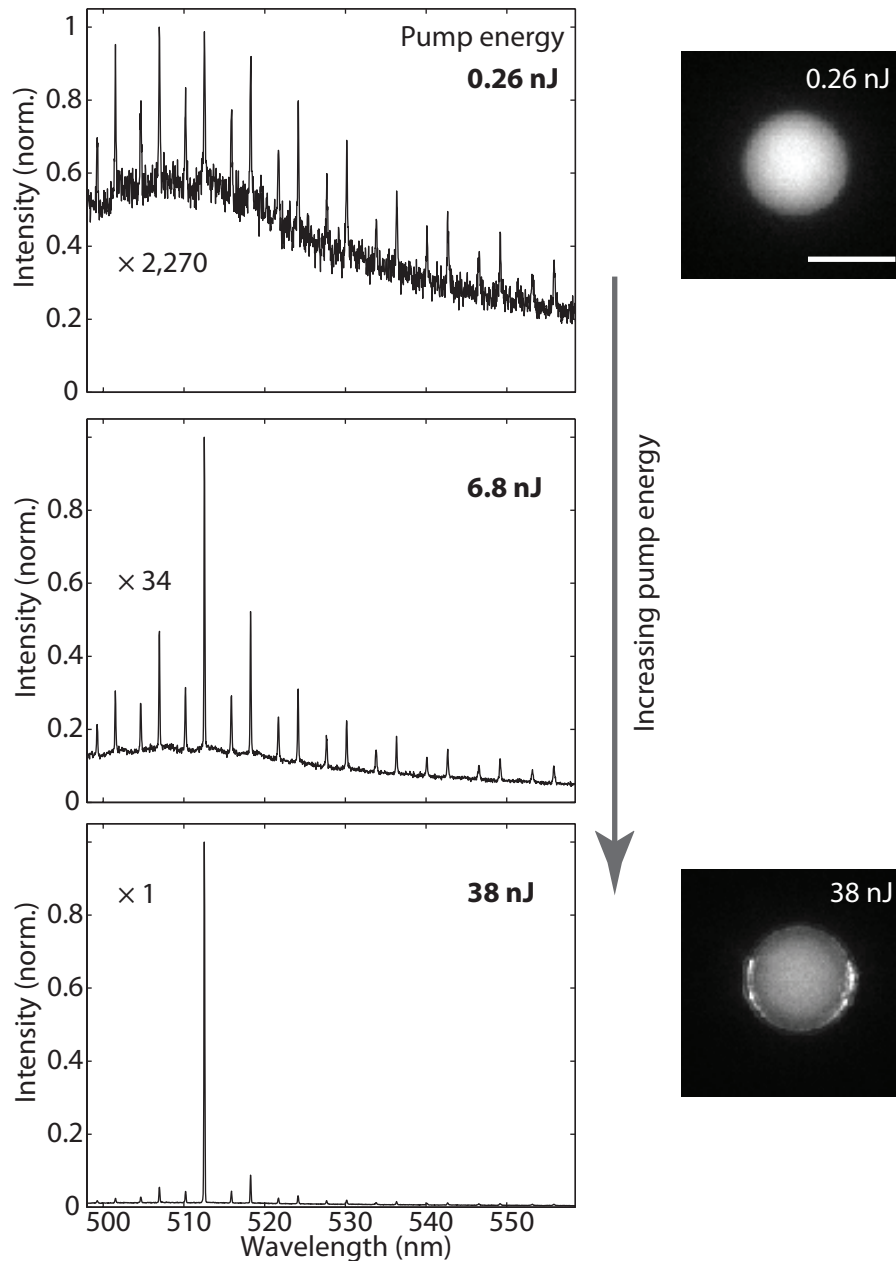
The spectral shift of a soda lime glass spherical bead of a given diameter when the surrounding refractive index is changed can be calculated using equation (1). For a diameter of 18 μ m, the spectral shift is 35 nm/RIU. We can track the position of WGM modes with a precision of 10 pm, which translates to a refractive index change of 2.9×10^{-4} . In the experiments we observed initial spectral shifts of the modes of 0.36 nm when increasing the osmolarity (Fig. 4f), which corresponds to a 1.0×10^{-2} change in the refractive index. The addition of NaCl also increase the refractive index of the medium by 3.6×10^{-4} and the corresponding mode shift is 1.3×10^{-2} nm, which is approximately 30 times less than observed.

References

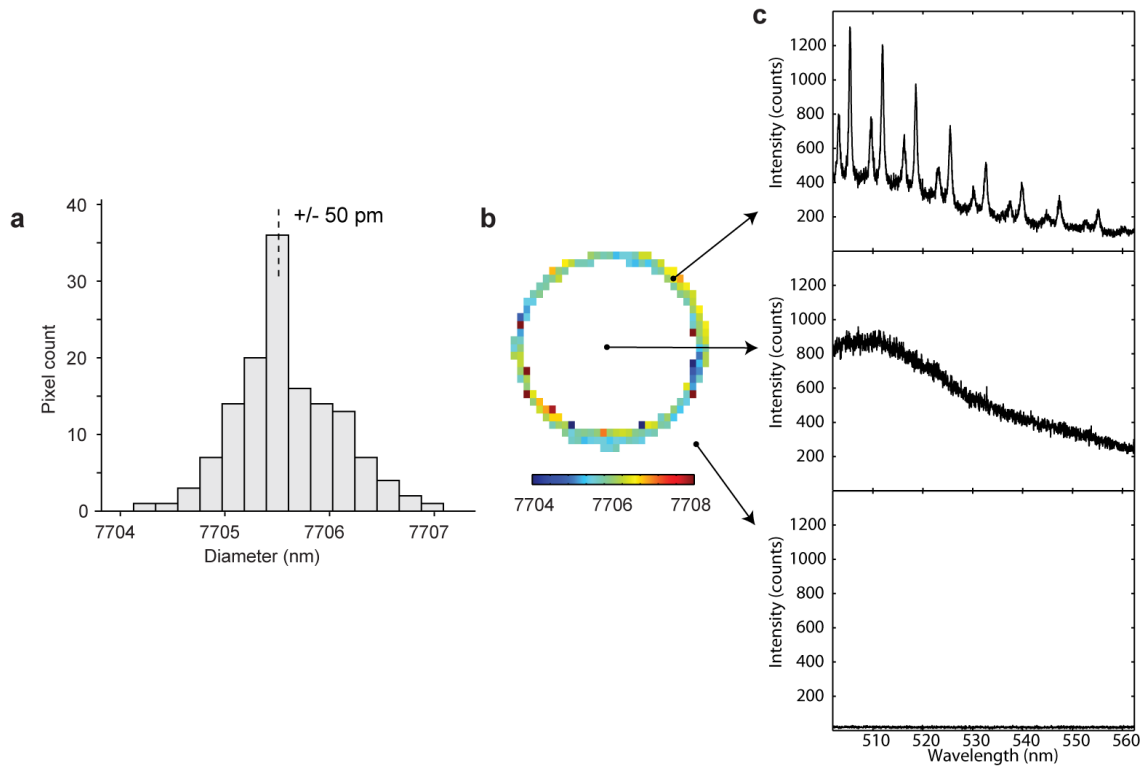
1. Gorodetsky M.L., Fomin A.E. Geometrical theory of whispering-gallery modes. *IEEE J. Sel. Topics Quantum Electron.* **12**, 33-39 (2006).
2. Datsyuk V. Some characteristics of resonant electromagnetic modes in a dielectric sphere. *Applied Physics B* **54**, 184-187 (1992).
3. Tivey D., Simmons N., Aiton J. Role of passive potassium fluxes in cell volume regulation in cultured HeLa cells. *The Journal of membrane biology* **87**, 93-105 (1985).
4. Lue N., *et al.* Live Cell Refractometry Using Hilbert Phase Microscopy and Confocal Reflectance Microscopy. *The Journal of Physical Chemistry A* **113**, 13327-13330 (2009).



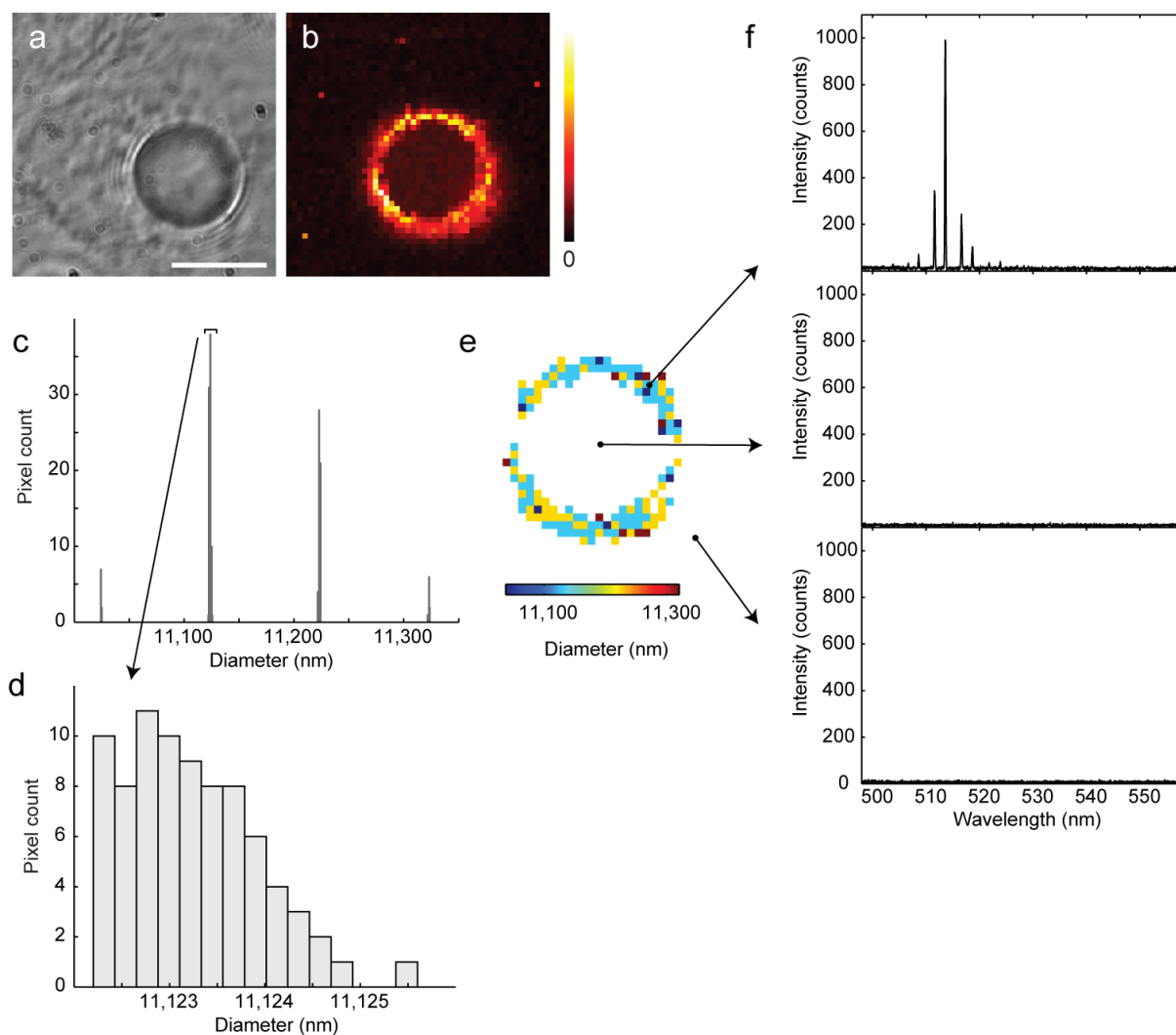
Supplementary Figure 1 | Adipocyte tissue from mouse. Subcutaneous adipocyte tissue was collected from the back of a mouse and stained with Nile red dye. Lasing was observed from droplets (arrows).



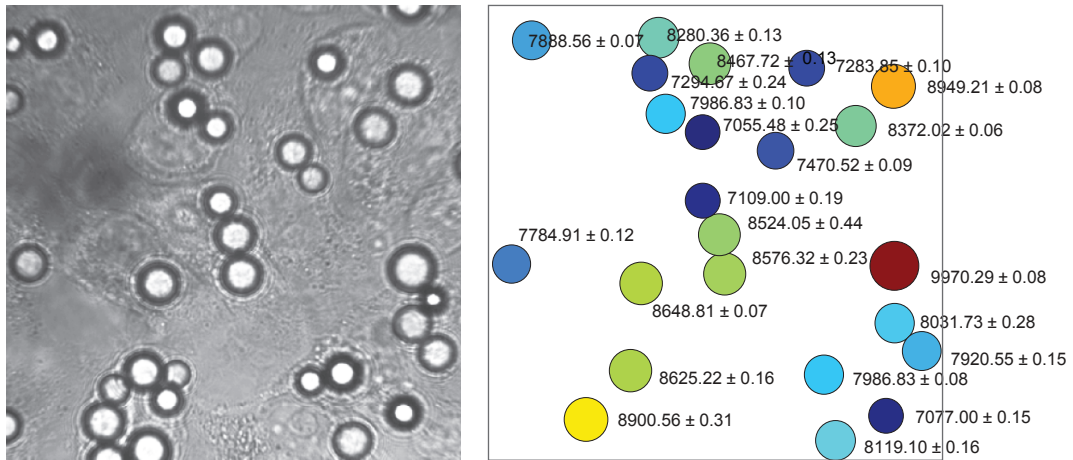
Supplementary Figure 2 | Spectrum from a fluorescent bead at different pump intensities. Spectrum below and above lasing threshold (2.4 nJ) for a polystyrene bead immersed in water. Below lasing threshold the WGMs are visible as peaks extending above fluorescent background. Above the threshold the peaks begin to dominate the spectrum with the fluorescent background barely visible. Insets: Below lasing threshold the bead is uniformly illuminated by the laser. Above the threshold a characteristic increase in the light intensity at the rim is observed. Scale bar, 10 μm .



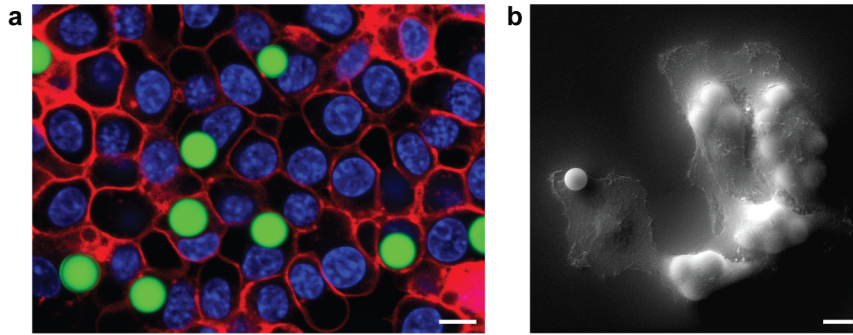
Supplementary Figure 3 | Measurement of the mode diameter of a bead below lasing threshold. **a**, Histogram of all the points in the diameter map in **b**. **c**, Spectra taken from three different points on the hyperspectral image.



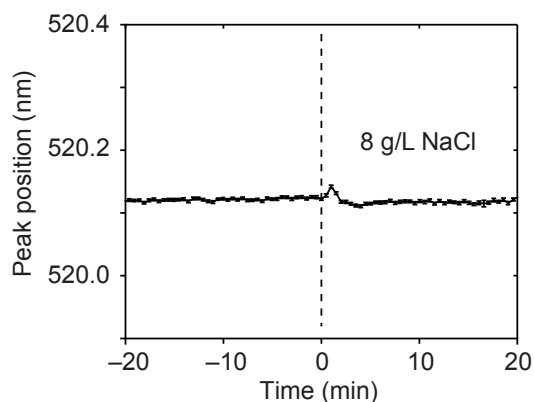
Supplementary Figure 4 | Measurement of the mode diameter of a bead in lasing regime. a, Bright field image of a HeLa cell containing a polystyrene fluorescent bead. **b,** False colour image of the cell, representing intensity of lasing WGMs. Integration time was 0.2 s per pixel, average over two pump pulses. **c,** Histogram of the bead diameter calculated from all the points in the hyperspectral image in (b). The calculated bead diameters fall into four distinct groups separated by ~ 100 nm corresponding to the free spectral range of the mode structure. Whenever the number of lasing modes is less than 3 to 4, the fitting algorithm is unreliable and does not always accurately produce correct mode numbers. (Below threshold in a non-lasing regime, such a problem is avoided since there are more modes available for fitting; see Supplementary Fig. 3). **d,** Zooming in on one of the groups shows an remarkably narrow diameter distribution with a width of only 2 nm. **e,** Calculated diameter map. **f,** Spectra taken from three different points on the hyperspectral image.



Supplementary Figure 5 | Diameter of beads calculated from their hyperspectral images. The number next to each polystyrene bead represents its average diameter and standard deviation error (\pm) in nanometres.



Supplementary Figure 6 | Fluorescent beads uptake by cells. **a**, Confocal image of RAW murine macrophage cells. Green: fluorescent beads, blue (Hoechst): cell nucleus, red (DiD dye): cell membrane. **b**, A SEM image of HeLa cells. Four cells on the right side contain 3-6 beads each. Scale bars, 10 μm .



Supplementary Figure 7 | Control experiment for sensing measurement. Position of a resonant peak from a glass bead inside a HeLa cell. A small quantity of phosphate buffered saline (PBS) was added to the cell growth medium with similar NaCl concentrations at $t=0$. The injection induced a small but measureable perturbation in $t=0$ to $t=2$ min. This measurement represents a control for the data in Fig. 4f in the text.

Supplementary Video 1 | (separate file) Microinjection of PPE droplets to NIH3T3 cells.

Real time video of the semiautomated injection of high index oil into cells. Some of the cells in the video were already injected with droplets. A standard glass micropipette with 1 μm tip was used for cell injection. Because of higher viscosity of the PPE oil higher pressures were used than normally for cell injections.

Supplementary Video 2 | (separate file) Hyperspectral video of fluorescent polystyrene beads inside HeLa cells.

High resolution spectra were recorded in each pixel of the view field containing multiple cells. The resulting hyperspectral image can be shown as a video with the wavelength changing in time. The beads show up as bright spheres in the same way as they would on a fluorescence image. However, at particular wavelength a bright ring is observed around a bead corresponding to a resonant mode. For larger spheres these flashes are more frequent and shorter corresponding to higher Q-factor. From the spectral positions of these modes, diameter of the beads can be measured down to 50 pm precision.